ACS Catalysis

pubs.acs.org/acscatalysis
Research Article

Tracking Sulfur Poisoning of Pd/Al_2O_3 Catalysts for Methane Oxidation on Different Complexity Scales

Tim Delrieux,[⊥] Shweta Sharma,[⊥] Florian Maurer, Joachim Czechowsky, Camelia Nicoleta Borca, Dmitry Karpov, Camilo Cárdenas, Patrick Lott, Maria Casapu, Thomas L. Sheppard,* and Jan-Dierk Grunwaldt*

Cite This: ACS Catal. 2025, 15, 13470−13485
Read Online

ACCESS | Metrics & More | Article Recommendations | Supporting Information

ABSTRACT: Understanding the deactivation induced by sulfur poisoning is crucial for designing more efficient palladium-based monolithic catalysts for methane oxidation. This study employs advanced characterization techniques, including X-ray absorption spectroscopy (XAS), X-ray fluorescence (XRF), spatially resolved activity measurements (SpaciPro), and synchrotron X-ray tomography, to investigate the effects of sulfur poisoning and regeneration from the atomic to the reactor scale. This includes structural changes, *i.e.*, oxidation state and chemical speciation in axial direction of a catalyst bed/coated monolithic channel as well as in the coated catalyst layer. Integral activity and spatially resolved kinetic measurements revealed that sulfur significantly reduces the catalytic activity for methane oxidation, in particular, from the beginning of the channel/catalyst bed. Gradients in sulfur concentration were observed along the axial direction of the coated channel of the monolithic honeycomb catalysts by XRF, supported by XAS. At the meso scale, X-ray holotomography provided three-dimensional (3D) maps (~400 μm diameter) uncovering some heterogeneous sulfur distribution within the catalyst layer due to different porosity/material structure. The sulfur gradients correlate with the catalytic activity as a function of the axial position of the reactor as uncovered by SpaciPro. Complementary XAS analysis at the S K-, Pd K-, and L_3-edges uncovered details on the chemical structure changes (*i.e.*, changes in Pd and S oxidation states) during poisoning and regeneration leading to loss of catalytic activity. They show that it is challenging to fully regenerate the Pd catalyst and its activity by a mild reductive treatment, particularly after prolonged sulfur exposure, as sulfur predominantly remains in its oxidation state +6. The insights obtained allow for quantifying sulfur-induced deactivation in technical catalysts as a function of composition and the location in the reactor. The insights may be used to develop and assess more stable catalysts in the future.

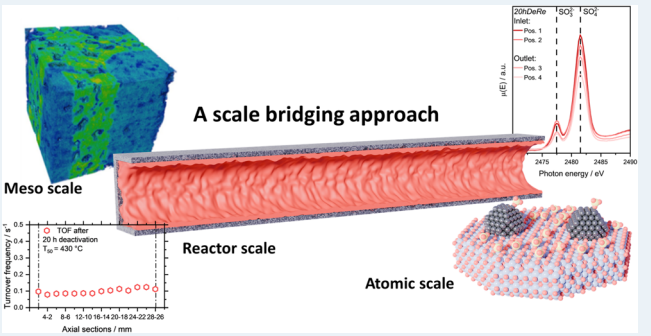

KEYWORDS: *methane oxidation, sulfur poisoning, palladium, structured catalyst, X-ray holotomography*

1. INTRODUCTION

Natural gas, which is mostly composed of methane, is often considered as a transition energy source due to its high fuel efficiency. The high hydrogen-to-carbon ratio of CH_4 results in lower carbon dioxide emissions in natural gas turbines and engines compared to those with the use of coal or crude oil as fossil fuels. Moreover, nitrogen oxides (NO_x) and particulate matter (PM) emissions are usually lower for natural gas than in comparable applications such as diesel or gasoline engines.[1−4] The use of methane is further being considered in the energy transition as it can be produced also in a CO_2-neutral manner via power-to-X processes and as sustainable biogas.[5,6] However, unburned CH_4 possess a 20 times higher global warming potential (GWP) when compared to CO_2, making an efficient exhaust gas aftertreatment system mandatory.[7]

As the most stable alkane, CH_4 is difficult to convert fully to CO_2 in typical combustion processes.[8,9] Pd-based catalysts show the highest catalytic activity at lower temperatures for the total oxidation of CH_4.[8,10−12] Nonetheless, the ongoing challenge in the design of long-term stable catalysts is their pronounced deactivation during operation.[12,13] The two most important deactivation mechanisms are deactivation by water and sulfur poisoning.[14−18] While water deactivation is reversible and intrinsic to the oxidation of CH_4 caused by the blockage of active sites by hydroxyl groups, sulfur poisoning leads to the sulfation of both the active metal and

Received: April 21, 2025
Revised: June 19, 2025
Accepted: June 20, 2025
Published: July 21, 2025

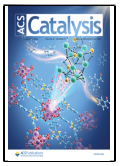

the support. Sulfur in the form of H_2S or SO_2 can originate from the natural gas itself, from added odorants in commercial fuel, or from biogas. Pd oxidizes the sulfur compounds to SO_3, and in the presence of water, to H_2SO_4, leading to the formation of stable and catalytically inactive $PdSO_4$ as well as to various S-containing compounds due to the spillover onto the support material.[19] Supports such as γ alumina (γ-Al_2O_3) are assumed to have high sulfur storage capacity due to their high surface area, thus prolonging the lifetime of the catalyst in sulfur-containing atmospheres.[20−22] Gremminger et al.[23] have reported that larger amounts of sulfur are stored at the upstream position of the catalyst, suggesting that the poisoning process gradually advances as a function of sulfur exposure time. S poisoning can be overcome to some degree by regenerative treatments with reductive gases or catalyst operation under rich conditions. Such treatments allow for temporarily recovering the catalytic activity, which strongly depends on the applied temperature, as shown by Lott et al.[24] While around 450 °C mostly the noble metal is regenerated, temperatures of up to 750 °C are needed to fully remove the sulfur stored on the support.[14,25] In the case of alumina, the sulfur storage capacity leads to a reverse spillover from the support to Pd, making regeneration more difficult.

Many efforts have been devoted to understand and improve the stability of methane oxidation catalysts at the atomic level and also on a larger scale, but only to a limited extent in the context of sulfur deactivation in technical catalysts.[14,23,24,26,27] In particular, for designing sulfur-resistant catalysts, a deeper and multidimensional scale-bridging understanding of the deactivation mechanism in technical catalysts needs to be generated. Technical catalysts such as washcoated monolithic honeycombs are heterogeneous in nature, which makes a complementary characterization approach mandatory. The influence of sulfur on the macro, meso, and atomic scale of the washcoated monolithic honeycombs is all relevant to technical catalyst performance. This study aims to elucidate the effects of sulfur poisoning on technical catalysts as a function of exposure time, and to determine the state of the catalysts after mild regeneration treatments in H_2-rich atmosphere. A series of Pd/Al_2O_3 catalysts were washcoated onto monolithic honeycombs and exposed to sulfur-containing atmospheres for different durations, followed by subsequent regeneration treatments in H_2. This procedure was used to investigate the propagation of the deactivation through a monolithic honeycomb. To reveal structural changes in the temporal and spatial dimensions within the catalyst, complementary characterization techniques, including X-ray absorption spectroscopy (XAS), spatially resolved activity measurements, and X-ray tomography, were applied to address all relevant length scales in a complementary manner. By addressing each of these scales, a knowledge-based design of more sulfur-resistant methane oxidation catalysts is potentially achievable through in-depth monitoring of the deactivation process.

2. EXPERIMENTAL SECTION

2.1. Catalyst Synthesis. The 2 wt % Pd/Al_2O_3 catalyst was prepared by multistep incipient wetness impregnation. In a first step, a commercial γ-Al_2O_3 support (Puralox TH 100/150, Sasol) was impregnated with an aqueous tetraamminepalladium(II) nitrate solution (5 wt %, abcr GmbH). The solution was added dropwise to alumina under constant mixing. This step was repeated 8 times until the desired Pd loading was achieved. The resulting powder was dried at atmospheric pressure in static air at 70 °C for 8 h and afterward calcined at 500 °C for 5 h under static air. The aqueous slurry of the catalyst powder was then coated onto a monolithic honeycomb (NGK, 500 CPSI, 3.5 mil) with a length of 3 cm and a diameter of 2.54 cm using several dip-coating steps until the desired loading of approximately 80 $g_{Pd}\cdot ft^{-3}$ was achieved.[28] Finally, the coated honeycomb was calcined at 550 °C under static air for 5 h.

2.2. Light-Off/Light-Out Experiments and Catalyst Deactivation. For the catalytic testing, the coated honeycombs were placed in a steel counter-current flow reactor (26 mm i.d.). The temperature of the reaction was monitored by two thermocouples placed upstream and downstream of the honeycomb at approximately 0.3 cm distance. The heating and cooling of the reactor was controlled by Eurotherm controllers using the thermocouple positioned in front of the catalyst bed. The gases for the reaction were dosed via Bronkhorst mass flow controllers (MFC), while water was dosed with a controlled evaporation mixing unit (CEM, Bronkhorst). The concentrations of the reactor outlet gases were analyzed with a Fourier transform infrared (FTIR) spectrometer (Multigas 2030, MKS).

All investigated samples were first degreened at 550 °C in 3200 ppm of CH_4, 10 vol % O_2, and 12 vol % H_2O in N_2 for 1 h before testing. The gas hourly space velocity (GHSV) was kept constant at 30,000 h^{-1}. In total, 7 different samples were selected, tested, and characterized:

i. *0hDe (zero hour deactivation):* Two consecutive light-off/light-out cycles were performed between 150 and 550 °C with a heating rate of 5 $K\cdot min^{-1}$, same gas mixture as for degreening step.
ii. *1hDe (1 h deactivation):* After applying the same 0hDe procedure, the reactor was cooled to 450 °C followed by a 60 min deactivation step with 2.5 ppm of SO_2, 3200 ppm of CH_4, 10 vol % O_2, and 12 vol % H_2O in N_2. Finally, the reactor was cooled down in this SO_2-containing reaction mixture.
iii. *1hDeRe (1 h deactivation and regeneration):* The sample was treated analogous to the *1hDe* procedure, followed by a 5 min regeneration step in 2 vol % H_2 in N_2 at 450 °C (GHSV of 30,000 h^{-1}).
iv. *20hDe (20 h deactivation):* The sample was treated similarly to *1hDe* but with a 20 h deactivation step at 450 °C in 2.5 ppm of SO_2, 3200 ppm of CH_4, 10 vol % O_2, and 12 vol %H_2O in N_2.
v. *20hDeRe (20 h deactivation and regeneration):* The sample was treated analogous to the *20hDe* procedure, followed by a 5 min regeneration at 450 °C in 2 vol % H_2 in N_2.
vi. *20hDeSpaci:* For spatial profiling (SpaciPro) of the activity, the catalyst-coated honeycomb was deactivated at 450 °C for 20 h in a gas feed containing 2.5 ppm of SO_2, 3200 ppm of CH_4, 10 vol % O_2, and 12 vol % H_2O in N_2 at a GHSV of 80,000 h^{-1}.
vii. *WhPr (whole process)*: To evaluate the effects of consecutive catalyst deactivation/reactivation cycles, one coated catalyst sample was exposed to a 5 min deactivation step at 450 °C in 2.5 ppm of SO_2, 3200 ppm of CH_4, 10 vol % O_2, and 12 vol %H_2O in N_2 followed by all steps between (ii) and (v), with the addition of a light-off after every deactivation and regeneration step.

https://doi.org/10.1021/acscatal.5c02678
ACS Catal. 2025, 15, 13470−13485

2.3. Spatial Profiling (SpaciPro) of the CH_4 Conversion. To probe the influence of the sulfur poisoning on the differential catalytic activity, spatially resolved CH_4 conversion profiles were measured. For the spatially resolved measurements, *1hDe* and *20hDeSpaci* were used. The gas feed was adjusted to a GHSV of 30,000 h^{-1} containing 3200 ppm of CH_4, 10 vol % O_2 in Ar. Like the procedure described above, the temperature was slowly ramped until a CH_4 conversion of 50% was achieved. Upon achieving 50% CH_4 conversion, spatially resolved measurements were conducted. For spatial profiling a quartz glass capillary (outer diameter 170 μm, inner diameter 100 μm) was moved through the corner of a single central channel of the coated monolith denoted as "SpaciPro"-technique, a method that has been described, *e.g.*, in refs 29,30. The gas phase was sampled *ca.* every 2 mm along the catalyst channel and analyzed with a mass spectrometer (HPR20, Hiden Analytical). In addition, after the spatially resolved measurements of the washcoated catalysts, a 5 min regeneration step was applied at 450 °C with a GHSV of 30,000 h^{-1} consisting of 2 vol % H_2 in Ar. Afterward, the temperature was adjusted again to achieve 50% CH_4 conversion, followed by spatially resolved measurements.

2.4. N_2-Physisorption. *N_2-physisorption* at −196 °C was used to determine the specific surface area and pore volume according to Brunauer−Emmett−Teller (BET)[31] and Barrett−Joyner−Halenda (BJH)[32] methods, respectively. The measurements were conducted in an Autosorb iQ (Anton Paar) instrument. Prior to measurements, the samples were degassed at 300 °C under reduced pressure for 2 h. Adsorption isotherms were investigated in the pressure range of p/p_0 = 0.05 to 0.3 during adsorption.

2.5. Transmission Electron Microscopy (TEM). Catalyst powders were scraped from the surface of the honeycombs after the reaction and dispersed on copper grids covered with lacey carbon. The Pd particle size was determined by means of high-resolution scanning transmission electron microscopy (HR-TEM) in an FEI Titan 80−300 microscope operated at 300 kV. The Pd particle size for the different samples (counting >100 particles) was determined based on several HAADF-STEM images by using the Fiji[33] software distribution.

2.6. Holotomography. Sample sections for hard X-ray holotomography measurements were extracted from both the inlet and outlet sections of the washcoated monoliths in their fresh, tested, poisoned, or regenerated states. This enabled a precise examination of variations along the channel axis, along with a comparison of the inlet and outlet zones.[34] Cross sections or corners of dimensions of approximately 2 mm height and 350 to 400 μm in diameter were cut manually from the inlet and outlet of each monolith sample and mounted on a sample support for tomographic measurements. The samples were inspected under a microscope to confirm their structural integrity and correct attachment. X-ray holotomography was performed at beamline ID16A (ESRF-EBS, Grenoble, France), using a beam with an incident energy of 17.1 keV and samples under vacuum conditions. The radiographs were recorded with a lens-coupled CMOS camera with 6144 × 6144 pixels (binned 3 by 3) and an effective pixel size of 1 μm. 2000 projections were recorded over the 180° sample rotation with an exposure time of 200−250 ms (depending upon the sample) for each projection. The field of view for the measurements was 286 × 286 μm^2 with 140 nm pixel size in the reconstructed projections. The reconstruction of the individual phase maps starts with the classical Paganin approach.[35] The result of this step is used as a starting input for gradient optimization, which quickly converges to the global minimum in the solution space. This procedure employs in-house-developed codes (ESRF-EBS) written in GNU Octave and using ImageJ for graphical evaluation. The obtained tomograms contain information about the complex refractive index $\delta(r)$, from which the electron density (N_e) can be calculated as described in refs 36,37 and shown in eq (9) in the Supporting Information, Section 6.2. The distribution of N_e values in the data sets was analyzed with ImageJ and python scripts to differentiate between individual sample components (*e.g.*, void, monolith, washcoat). Details are given in Table 1, each representing different treatment conditions (i−vi above) for the monoliths with Pd/Al_2O_3.

Table 1. Sample Nomenclature for Holotomography Measurements

sample type	inlet position	outlet position
fresh	*F_in*	--
0hDe	*0hDe_in*	--
1hDe	*1hDe_in*	*1hDe _out*
20hDe	*20hDe_in*	*20hDe _out*
1hDeRe	*1hDeRe _in*	*1hDeRe_out*

2.7. Spatially Resolved *Ex Situ* X-ray Absorption Spectroscopy. *Ex situ* XAS measurements at the Pd K-edge (24,350 eV) were performed at the CAT-ACT beamline[38] (KIT light source, Karlsruhe) using a Si(311) double-crystal monochromator (DCM). The experiments were conducted in transmission mode at room temperature with Pd foil as the reference and Ar-filled ionization chambers. Additional X-ray absorption near-edge structure (XANES) measurements at the Pd L_3-edge (3173 eV) and S K-edge (2472 eV) were performed at the PHOENIX beamline (SLS, Villigen) using a 4-element silicon drift (SSD, VORTEX) detector in fluorescence mode under vacuum conditions (10^{-6} bar). The SSD detector has an energy resolution of 150 eV. For all investigations, 5 × 2 channels over the whole 3 cm length were cut out from the tested honeycombs and probed at two different points of the inlet and outlet positions. The obtained XAS were evaluated using the Athena software from the IFFEFIT software package.[39] Quantification of the noble metal species, *e.g.*, PdO, metallic Pd, $PdSO_4$, or PdS, was achieved by linear combination analysis (LCA) of the normalized XANES of reference compounds. The reference samples at the Pd L_3- and S K-edge were measured with a 1x 1 mm beam, while the samples were measured with a 50 μm × 50 μm beam with a dwell time of 1 s per point. The extended X-ray absorption fine structure (EXAFS) region of the Pd K-edge spectra was extracted in the k-range from 3 to 10 $Å^{-1}$ (k^2-weighted).

2.8. Spatially Resolved Synchrotron X-ray Fluorescence Measurements. X-ray fluorescence (XRF) measurements were performed at the PHOENIX beamline (SLS, Villigen) at 2480 and 3173 eV (just above S K-edge and Pd L_3-edge). The signals for S and Pd (fluorescence lines: Pd-L_α, S−K_α) were recorded along the cut out 5 × 2 channels with 3 cm length using an SSD detector (VORTEX) of the pretreated samples described above. The signals were normalized to the signal measured at the inlet position for the same sample.

2.9. Elemental Analysis of the Coated Catalyst. The stored amount of S during the deactivation and after the

https://doi.org/10.1021/acscatal.5c02678
ACS Catal. 2025, 15, 13470−13485

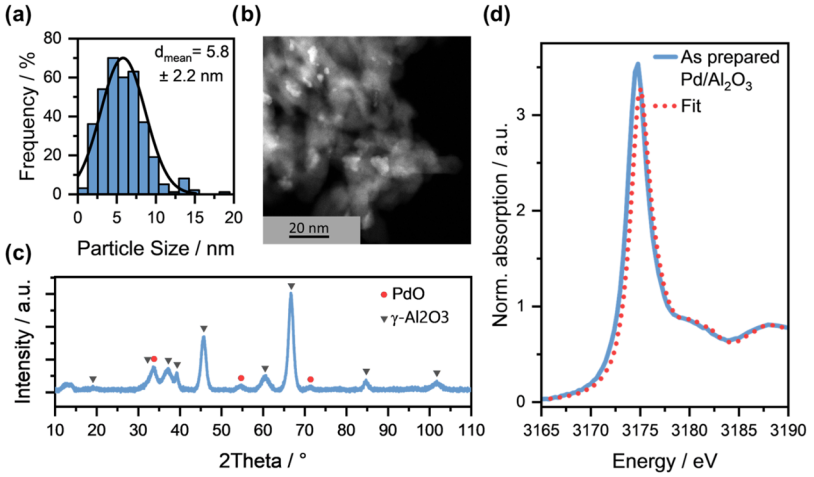

Figure 1. *Ex situ* characterization of as-prepared Pd/Al_2O_3 catalyst: (a) Particle size distribution based on the evaluation of approximately 300 particles; (b) HAADF-STEM image; (c) XRD patterns and (d) the Pd L_3-edge spectrum of the as-prepared catalyst with the corresponding fit using Pd and PdO as reference materials. Additional EDX analysis of the as-prepared Pd/Al_2O_3 is provided in the Supporting Information (Figure S1).

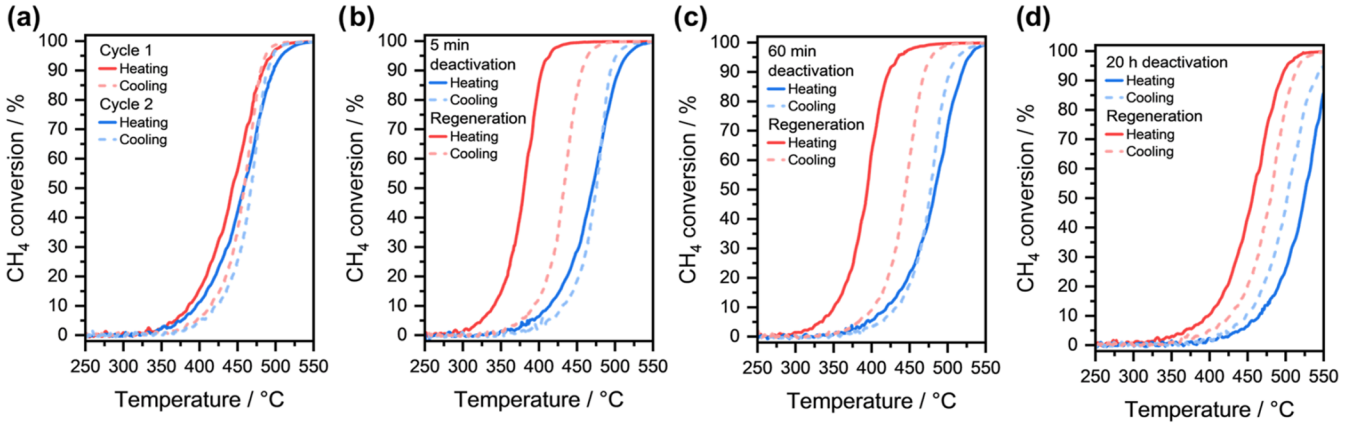

Figure 2. CH_4 conversion of the *WhPr* Pd/Al_2O_3 catalyst at a GHSV of 30,000 h^{-1} with 3200 ppm of CH_4, 10 vol % O_2, and 12 vol % H_2O in N_2 (a) after degreening, (b) after 5 min deactivation with 2.5 ppm of SO_2 and subsequent 5 min regeneration with 2 vol % H_2 in N_2 (both at 450 °C), (c) after 60 min deactivation and subsequent regeneration in the same way as for (b, d) after 20 h deactivation again in 2.5 ppm of SO_2 and subsequent regeneration with 2 vol % H_2 (both at 450 °C).

regeneration steps was determined by elemental analysis (EA) (2000 HT, Thermo Fisher Scientific) coupled to an isotope-ratio mass spectrometer (IRMS) (Delta V Advantage, Thermo Fisher Scientific). The measurements were calibrated to a sulfanilamide standard. An additional thermal conductivity (TCD) detector was used for the quantification of the S amount. Approximately 150 mg of the sample was weighed and combusted under an oxygen atmosphere. For the analysis, inlet and outlet sections (5 mm) of each Pd/Al_2O_3-coated honeycomb were ground into a powder.

3. RESULTS AND DISCUSSION

3.1. Integral CH_4 Conversion. The as-prepared 2 wt % Pd/Al_2O_3 catalyst was found to have a specific surface area of 132 $m^2 \cdot g^{-1}$, a pore volume of 0.85 $m^2 \cdot g^{-1}$, and a median pore diameter of 26 nm, making it mesoporous. Figure 1a shows the noble metal particle size distribution (PSD) based on HAADF-STEM analysis for the as-prepared Pd catalyst with an average particle size of 5.8 ± 2.2 nm. The corresponding HAADF-STEM image in Figure 1b shows the poorly crystalline shape of the Pd particles, which are homogeneously distributed over the Al_2O_3 support. The presence of larger PdO crystallites is also supported by the corresponding XRD patterns (Figure 1c), with sharp reflections at 2θ = 34, 55, and 72 °. The comparison of the Pd L_3-edge XANES of the as-prepared Pd catalyst with those obtained for the PdO and Pd foil references confirmed the oxidized state (>90%). The linear combination analysis indicates the presence of more than 90% of Pd^{2+} species.

The two consecutive light-offs (Figure 2a) of *WhPr* after the degreening step show similar activity profiles with 50% CH_4 conversion achieved at 445 and 460 °C (T_{50} temperatures), respectively. Next, 2.5 ppm of SO_2 was dosed for 5 min at 450 °C, resulting in a noticeable decline of the catalytic activity even for this very short treatment (Figure 3). With the 5 min deactivation step, the T_{50} temperature shifted upward to 470 °C (Figure 2b). Afterward, the regenerative treatment in 2 vol % H_2 at 450 °C resulted in a significant improvement of the catalytic activity. In this case, the lower T_{50} of 370 °C is caused not only by the sulfur removal but especially by the depletion of the OH groups during the reduction of Pd particles, as shown by Lott et al.[40] This effect is confirmed by the deactivation under reaction conditions during the following

https://doi.org/10.1021/acscatal.5c02678
ACS Catal. 2025, 15, 13470−13485

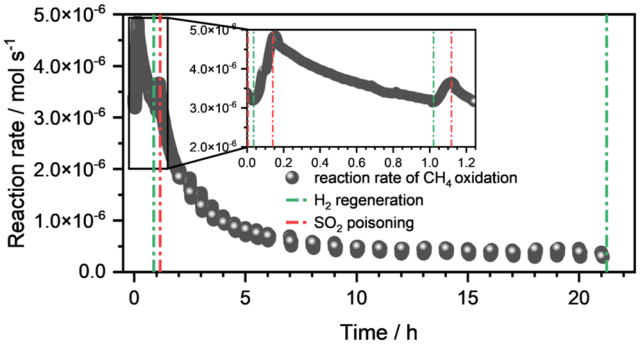

Figure 3. Reaction rate of methane oxidation as a function of time during sulfur poisoning with 2.5 ppm of SO_2 in N_2 at 450 °C for 5 min, 60 min, and 20 h (Start of S poisoning is indicated by red line). After each deactivation step, a regeneration treatment with 2 vol % H_2 in N_2 for 5 min at 450 °C with a GHSV of 30,000 h^{-1} was applied (cf. procedure for *WhPr*, indicated by the green lines). The green lines indicate the start of the H_2 regeneration treatment, and the red lines indicate the start of the SO_2 poisoning.

light-out, displaying a T_{50} of ∼430 °C. Additional catalytic data during S poisoning of *1hDe* and *20hDe* are given in the Supporting Information.

In a next step, the washcoated Pd/Al_2O_3 catalyst was further deactivated for 60 min with 2.5 ppm of SO_2 at 450 °C, with a subsequent regeneration treatment in 2 vol % H_2 at 450 °C. T_{50} increased further to 485 °C due to the SO_2 deactivation (Figure 2c) but could be recovered (T_{50} = 400 °C) with the subsequent regeneration. Lastly, a 20 h deactivation step was applied to severely deactivate the catalyst until a minimum reaction rate was observed (Figure 3), to study the catalyst once the S storage capacity is depleted and the catalyst is fully saturated with sulfur. The T_{50} measured during the subsequent light-off period increased to about 525 °C (Figure 2d), with incomplete CH_4 conversion observed at a maximum temperature of 550 °C (Figure 2d). In this case, the reductive treatment applied to regenerate the catalyst caused only a partial recovery of the catalyst activity, *i.e.*, T_{50} of CH_4 oxidation of 460 °C.

Generally, while water deactivation leads to the appearance of an inverse hysteresis profile during CH_4 oxidation light-off/light-outs, a typical hysteresis (higher activity during light-out) is increasingly visible as the SO_2 poisoning time is enhanced (*e.g.*, *20hDeRe* in Figure 2d). The different T_{50} values are summarized in Figure 4. After the reductive regeneration, the hysteresis loop is again reversed and a lower activity is noticed during the light-outs. This tendency is probably caused by the concurrent contributions of water deactivation and SO_2 spillover (*e.g.*, *1hDeRe* in Figure 2c), which is discussed next in more detail.

The minor decrease in catalytic activity observed during cycles 1 and 2 in Figure 2a indicates minor deactivation by hydroxyl groups formed on the catalyst surface or even the formation of $Pd(OH)_2$, due to the water present in the gas feed and its inherent formation during the reaction.[17,41−43] In addition, water could promote the sintering of the Pd particles, leading to a decrease in the number of active sites.[44] However, water deactivation plays overall a minor role compared with the pronounced SO_2 poisoning effect. This becomes obvious in the case of the 5 min deactivation treatment with 2.5 ppm of SO_2 at 450 °C. As shown in Figure 3, an accelerated decrease in reaction rate can be observed as soon as sulfur is dosed, clearly indicating that the overall deactivation of the catalyst is governed by sulfur poisoning. The Pd at the upstream positions of the catalyst oxidizes SO_2 in the presence of water to H_2SO_4, probably leading to the formation of stable and catalytically inactive $PdSO_4$. Nevertheless, due to the rather short deactivation time, only a fraction of the Pd noble metal is affected, resulting in a minor decrease in catalytic activity, while a larger fraction of the Pd remains active. On the other hand, the sulfur storage capacity of Al_2O_3 may mitigate the decrease in catalytic activity, as some of the sulfur is spilled over onto the Al_2O_3 support, thus preventing sulfur from reacting with Pd. The improved catalytic activity following the regeneration step can be also attributed to several phenomena. Hydrogen efficiently removes the formed hydroxyl groups from the Pd surface and restores the active sites. In addition, Lott et al.[40] have shown that the pre-reduction of Pd can have a positive impact on the overall methane oxidation activity due to highly active PdO-Pd species that form during the subsequent light-off. Similar results were reported by Franken et al.,[45] who showed that short reducing pulses continuously remove surface hydroxyls, while facilitating the formation of highly active PdO_x-Pd phases. Furthermore, H_2 was shown to reduce PdO at first to metallic Pd and then further to PdS, which decomposes to PdO when exposed to O_2 during the subsequent light-off, leading to the recovery of the catalytic activity.[14] The catalytic activity then decreases again during the light-out, which can be attributed again to surface hydroxyls and also due to the total oxidation of Pd, leaving the catalyst in a less active state.[45,46] In addition, sulfur stored on the alumina support can reverse spillover to the noble metal, further decreasing the catalytic activity. This trend continues for 60 min and 20 h of deactivation. The deactivation front probably advances through the washcoated catalyst, leaving more Pd

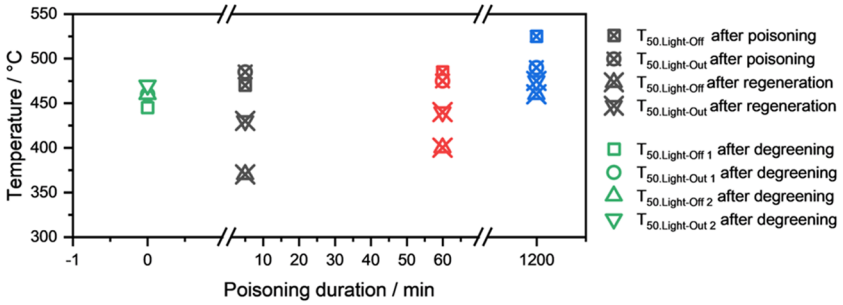

Figure 4. Summary of the different T_{50}'s for the light-off and light-out of *WhPr* after the degreening (green, nonpoisoned), 5 min deactivation (gray), 60 min deactivation (red), and 20 h deactivation (blue).

https://doi.org/10.1021/acscatal.5c02678
ACS Catal. 2025, 15, 13470−13485

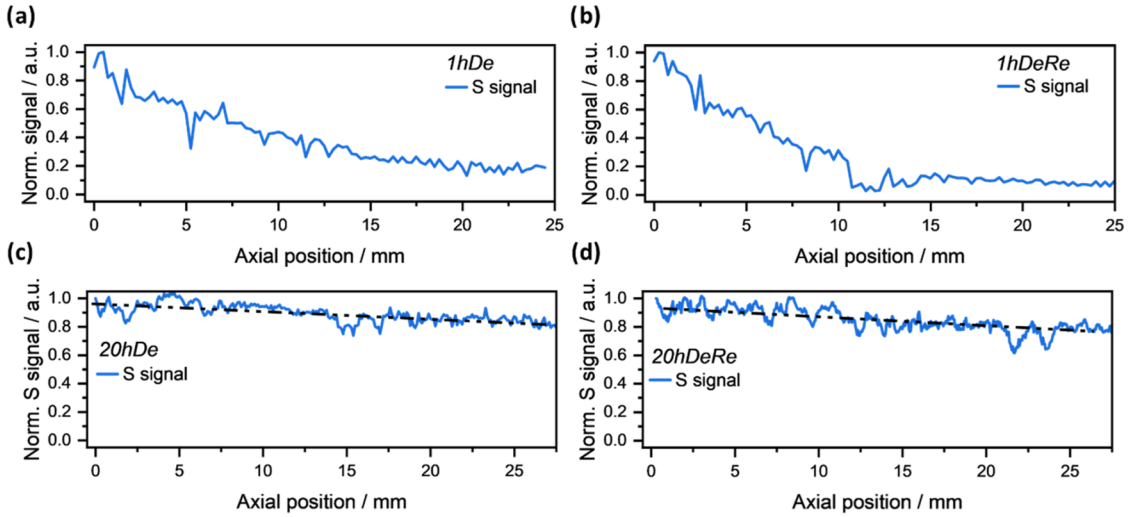

Figure 5. XRF measurements along the catalyst at the S K-edge (2480 eV) showing S−K_α fluorescence lines normalized to the inlet signal. (a) *1hDe*, (b) *1hDeRe*, (c) *20hDe*, and (d) *20hDeRe*.

deactivated. Since a minimum in reaction rate is observed after 8 h on stream in the case of the *20hDe* procedure (Figure 3), it can be assumed that the majority of Pd sites reacts with SO_2. Simultaneously, more sulfur is stored on the alumina support after each deactivation step, which decreases the catalytic activity during the light-out after the regeneration treatment due to the reverse spillover onto the Pd. The slight improvement in activity during light-out after each deactivation step could be caused by partial desorption of S at elevated temperatures during the light-off.

Overall, the observed changes in the integral CH_4 oxidation activity as a function of the SO_2-poisoning time suggest gradual variations in the Pd catalyst oxidation state along the reactor in the direction of the gas stream and in the catalyst layer. However, previous studies have mainly focused on the active species during sulfur poisoning, without specifically accounting for spatial effects within the context of a technical catalyst systems including their regeneration.[14,47] The complex and hierarchical nature of such technical systems requires a spatially resolved approach across the length and complexity scales.

3.2. Spatial Evolution of the Sulfur Poisoning within the Monolithic Channels. To determine the sulfur concentration in the axial direction of the coated honeycomb, a section of 5 × 2 channels with a 30 mm length was extracted from the tested samples. Figure 5 shows the XRF analysis (S−K_α fluorescence lines) at 2480 eV (just above the S K-edge) along the honeycomb channels. In addition, the Pd-L_α fluorescence signal along the honeycomb shows a homogeneous distribution of Pd along the catalyst bed (Supporting Information). This also indirectly shows the uniformity of the catalyst layer after the dip-coating procedure within the penetration depth of the soft X-ray. Hence, this characterization approach allows to relate the observed trends directly to the catalyst treatment (deactivation/reactivation), while minimizing possible effects from the coating procedure itself. While the absolute values of the XRF signal are provided in the electronic Supporting Information (Figure S3), here the normalized values are discussed (Figure 5).

In general, the results show that the amount of sulfur-containing species decreases toward the outlet of the catalyst-coated channel for all investigated samples, regardless of the treatment history. After the 60 min SO_2 poisoning (*1hDe* in Figure 5a), a strong gradient with an S signal drop to 20% along the axial direction of the 8 mm long catalyst monolith channel can be observed. This trend is even more pronounced after the following 5 min regeneration in 5% H_2/N_2 at 450 °C (*1hDeRe* in Figure 5b). In this case, the normalized S−K_α signal decreases to a minimum already at the middle of the coated catalyst, demonstrating that the SO_2-poisoning gradually develops along the catalyst bed. In contrast, for the longest SO_2-deactivated sample (*20hDe* in Figure 5c), a linear decrease of sulfur species was found from the upstream to downstream positions. Interestingly, a similar trend was identified for *20hDeRe* (Figure 5d). However, the overall S concentration decreased by approximately 5%. A general explanation for the variations in the slopes of the S fluorescence signal between the samples could be the different S-storage capacities from sulfation of the alumina support via SO_2 oxidation, along with S-spillover effects from Pd sites. Due to its high surface area, γ-alumina is known to store larger amounts of sulfur as sulfites or sulfates in comparison to other supports like ceria or zirconia, thus also delaying the Pd deactivation.[20,48,49] Despite the temporary nature of this mitigation effect, the ability to store sulfur is especially pronounced in comparison to other nonsulfating supports such as SiO_2-based materials, which lead to a significantly faster loss in the activity of CH_4 oxidation catalysts compared to Pd/Al_2O_3 tested here.[50,51] In the Pd/Al_2O_3 catalyst investigated in this study, sulfur storage starts upstream of the catalyst channel. The larger differences between upstream and downstream positions occur during initial/short SO_2-exposure periods, and their differences in the S concentration remain almost unchanged after the H_2-reductive regeneration step. This behavior is due to the relatively low regeneration temperature of 450 °C, which is probably sufficient only for the regeneration of the noble metal species while the full recovery of the alumina support is not expected.[14] As the noble metal loading is only 2 wt %, S removal from/around Pd sites only results in small changes in the overall S concentration. This supports the idea that changes in S content due to regeneration can be subtle and, therefore, challenging to observe without spatially resolved methods.

https://doi.org/10.1021/acscatal.5c02678
ACS Catal. 2025, 15, 13470−13485

To quantify the amount of sulfur stored and to confirm the trend in S concentration uncovered by the XRF investigations, elemental analysis was conducted at the inlet and outlet of the coated catalysts (approximately 5 mm into the honeycomb). Table 2 shows the total amount of dosed S as a function of

Table 2. Quantification of Sulfur Content Located at Inlet and Outlet of the Monolithic Honeycombs

	total amount of S dosed/mg	amount of S at inlet/mg·g^{-1} honeycomb	amount of S at outlet/mg·g^{-1} honeycomb
1hDe	3	0.23	0.03
1hDeRe	3	0.29	below detection limit
20hDe	60	2.98	2.74
20hDeRe	60	2.82	2.33

time during the different SO_2-poisoning procedures and the amount of deposited S as a function of the catalyst position. The results obtained confirm the higher concentration of S at the beginning of the catalyst bed, in agreement with the XRF data. Considering the estimated weight of the coated monolith channels and the total amount of S as derived from the elemental analysis, it can be concluded that independent of the deactivation time, only about 70% of the dosed sulfur is deposited on the catalyst. With respect to the application of technical catalysts, external transport limitations in the technical catalyst channels and potential gas bypass may account for this observation, especially given the low SO_2 amount in the gas feed. In this regard, the desorption of S-containing species does not play a significant role at the given temperature of 450 °C.[14]

3.3. Oxidation State and Structure of S and Pd. While the spatial XRF measurements provide details on the distribution of sulfur species within the monolithic channels, it is equally important to gain insights into the local structure, *i.e.*, Pd and S oxidation states. Figure 6 shows the XANES spectra collected at the S K-edge for the different samples and a schematic drawing of the monolith channel with the investigated positions (Figure 6a). By adjusting the pre-edge of the spectra to zero for better comparison and due to the constant beam size and dwell time, the local sulfur concentration and oxidation state based on the peak location can be qualitatively compared within the different samples. In line with the XRF measurements, the S K-edge around 2480.9 eV indicates the presence of S^{6+} species (SO_4^{2-}) in all samples (XANES data for reference samples, cf. Figure S4). In addition, at least for the upstream positions of all SO_2-poisoned samples, a well-defined pre-edge feature around 2477.5 eV is observed, indicating the formation of SO_3^{2-}.[52]

The formation of both aluminum sulfates and sulfites through the direct adsorption of SO_2 on Al_2O_3 has been reported for similar noble-metal-based catalysts, probably via the spillover of SO_3 from the noble metal sites.[53] The presence of these species in the SO_2-poisoned catalysts explains the similar profile of the S K-edge spectra after reductive treatment. As mentioned above, at 450 °C, primarily only $PdSO_4$ reacts with H_2 and not the sulfated Al_2O_3 support.[14]

Concerning the variations in sulfur species along the catalyst bed, a lower concentration of S species was not only noticed for *1hDe* and *1hDeRe* at the outlet positions, but the overall S amount was also diminished after the short reduction treatment (Figure 6b,c). At the same time, an increase in the intensity for the edge feature at 2477.5 eV and the appearance of new features at lower energy were found particularly at position 1 in the monolith channel, probably due to the formation of sulfides (S^{2-}) on the Pd surface during catalyst regeneration in H_2. Less pronounced structural variations were observed after 20 h of SO_2-poisoning. This is further underlined in Figure 6d,e for *20hDe* and *20hDeRe*. *20hDe* shows a more pronounced S K-edge jump for both upstream positions, which decreases for downstream positions. *20hDeRe* shows high amounts of sulfate after regeneration, confirming the spillover onto the support.

In the next step, complementary *ex situ* XAS investigations were conducted at the Pd L_3- and K-edges. The XANES spectra obtained at the Pd K-edge for the catalyst are depicted in Figure 7a–d. The corresponding reference spectra and EXAFS images are shown in Figure S11. Independent of the deactivation time, an oxidized state was identified for Pd at all positions in the catalyst bed after the SO_2-poisoning treatments. This is well in line with the literature due to the high similarity of the white line profiles for PdO and $PdSO_4$ bulk references, making the identification of the noble metal phase after SO_2 poisoning only based on the Pd K-edge XANES challenging. After the reductive treatment, a spectrum was obtained that shows more similarities to a reduced sample than to an oxidized one in both *1hDeRe* and *20hDeRe*. According to the LCA results, a mixture of Pd, PdO, and PdS is present in the regenerated catalysts. An overview of their different proportions along the monolith channels is reported in Table 3. For *1hDeRe*, an average amount of 21% PdS was found along the catalyst in the direction of flow, with the rest being 62% metallic Pd and 18% PdO. In the case of *20hDeRe*, an average amount of 34% PdS was found. The rest is composed of 56% Pd and 10% PdO. The overall lower amounts of PdS for *1hDeRe* is due the shorter deactivation time: Since less sulfur is stored, also less sulfur reacts with the noble metal to form catalytically inactive $PdSO_4$. The $PdSO_4$ then reacts with H_2 to form PdS, which is then oxidized during the subsequent light-off. The observed formation of PdS is also corroborated by EXAFS (Figure S11). Here, the comparison of EXAFS in R-space of metallic Pd to *1hDeRe* and *20hDeRe* shows a shift of the typical Pd–Pd peak at 2.6 Å to lower values, indicating the formation of PdS. The change in oxidation state during the SO_2-poisoning reaction is also accompanied by an increase in Pd particle size as seen in the TEM images in Figure 7e–h. After the degreening and the two consecutive light-offs (Figure 6e), the particles grew to a size of 8.4 nm from an initial 5.8 nm, preserving their shape as observed in Figure 1. This particle size remains constant at around 8 nm, independent of the subsequent sulfur poisoning or regeneration treatment.

Furthermore, in contrast to the Pd K-edge data, the L_3-edge spectra (Figure S12) are expected to allow a better detection of the changes in the Pd oxidation state after SO_2-poisoning. However, the short penetration depth of the incident beam (only ~0.6 μm probed) at the L_3-edge energy (3170 eV) limits the sensitivity of these measurements to the surface layers, increasing the inhomogeneity of the obtained results.[54] The LCA shows even amounts of Pd–S species along the direction of flow along the catalyst, with higher amounts of Pd–S species measured for the *20hDe*. This observation is in line with the findings at the Pd K-edge. However, the LCA for the regenerated samples shows fully reduced Pd for *1hDeRe* and small amounts (>10%) of PdS for *20hDeRe* toward the outlet. This can be explained by the above-mentioned penetration

https://doi.org/10.1021/acscatal.5c02678
ACS Catal. 2025, 15, 13470–13485

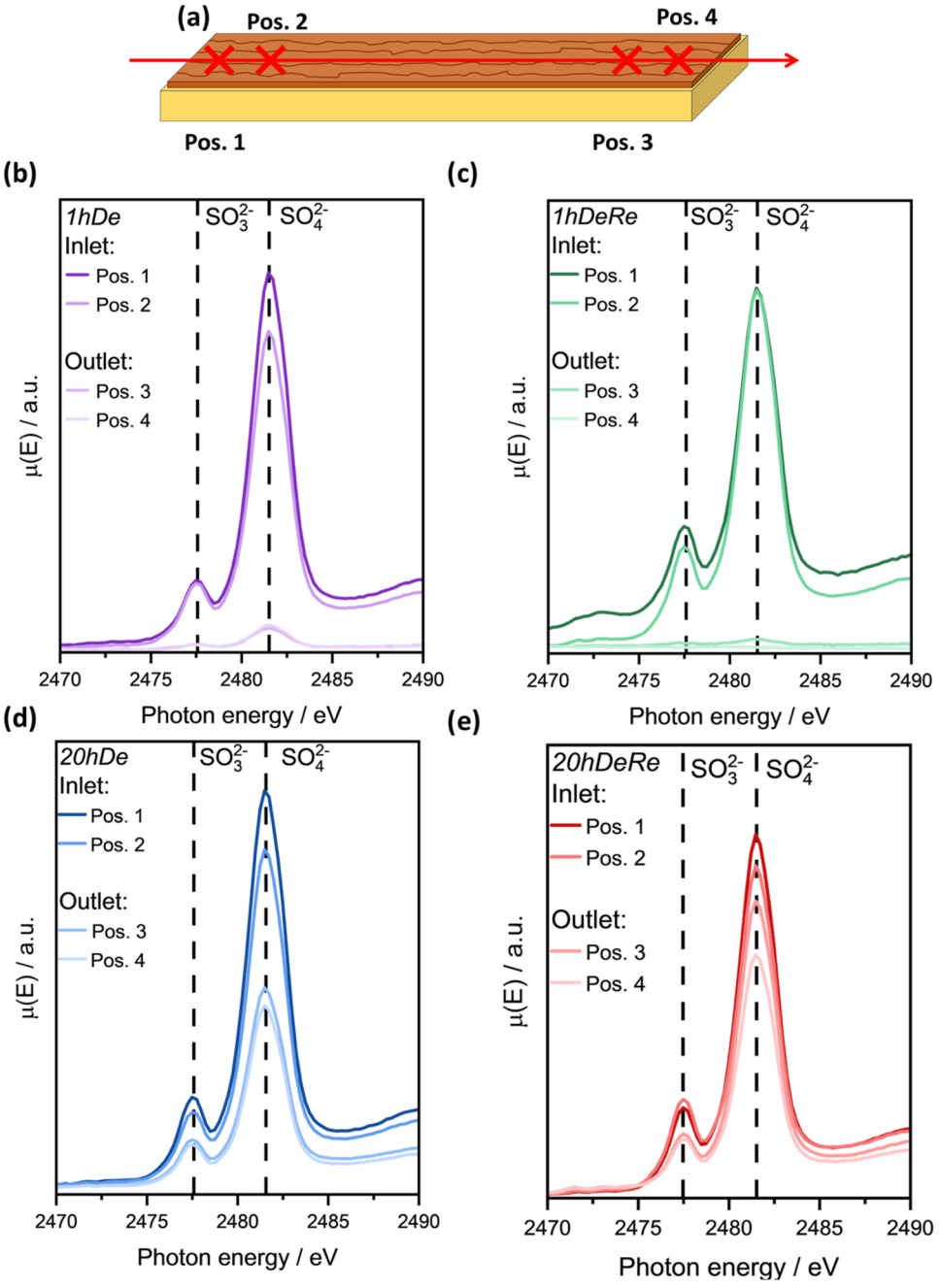

Figure 6. Schematic overview of measurement positions and XAS spectra recorded at the sulfur K-edge (2480 eV) at the inlet and outlet positions of the monolithic sample for different deactivation times with a stream containing 2.5 ppm of SO_2, 3200 ppm of CH_4, 12% H_2O, and 10 vol % O_2 in N2. (a) Schematic overview of the 2 × 5 measured monolith wall with Pos. 1−4 marking the measurement positions of the XANES spectra, (b) *1hDe*, (c) *1hDeRe*, (d) *20hDe*, and (e) *20hDeRe*.

depth of the beam. In addition to the K-edge spectra, the L_3-edge spectra emphasize further that the catalyst deactivation and regeneration should not be seen only in a single dimension. In realistic systems, deactivation and regeneration are dependent on the time and the directions along the monolithic catalyst and into the washcoat layer.

3.4. Noninvasive Spatial Profiling with X-ray Holotomography. The effects of sulfur poisoning revealed by XAS and XRF above provide crucial chemical and compositional insights into catalyst deactivation. However, they are mostly surface-sensitive when performed with soft X-rays with low penetration depth and are therefore limited in probing the whole catalyst layer. Holotomography is a noninvasive technique that complements these techniques by providing 3D volumes of the electron density distribution, offering a more comprehensive understanding of degradation, including bulk and local morphological and chemical changes.[55] Thus, hard X-ray holotomography was employed to attempt to visualize the effects of sulfur poisoning in the washcoated monolithic honeycomb samples. The volumes obtained by holotomography (cf. Supporting Information, shown in Figure S14) reveal a distinct separation between the cordierite (support material), the washcoat (active material), and the network of pores in each layer. This visualization highlights the

https://doi.org/10.1021/acscatal.5c02678
ACS Catal. 2025, 15, 13470−13485

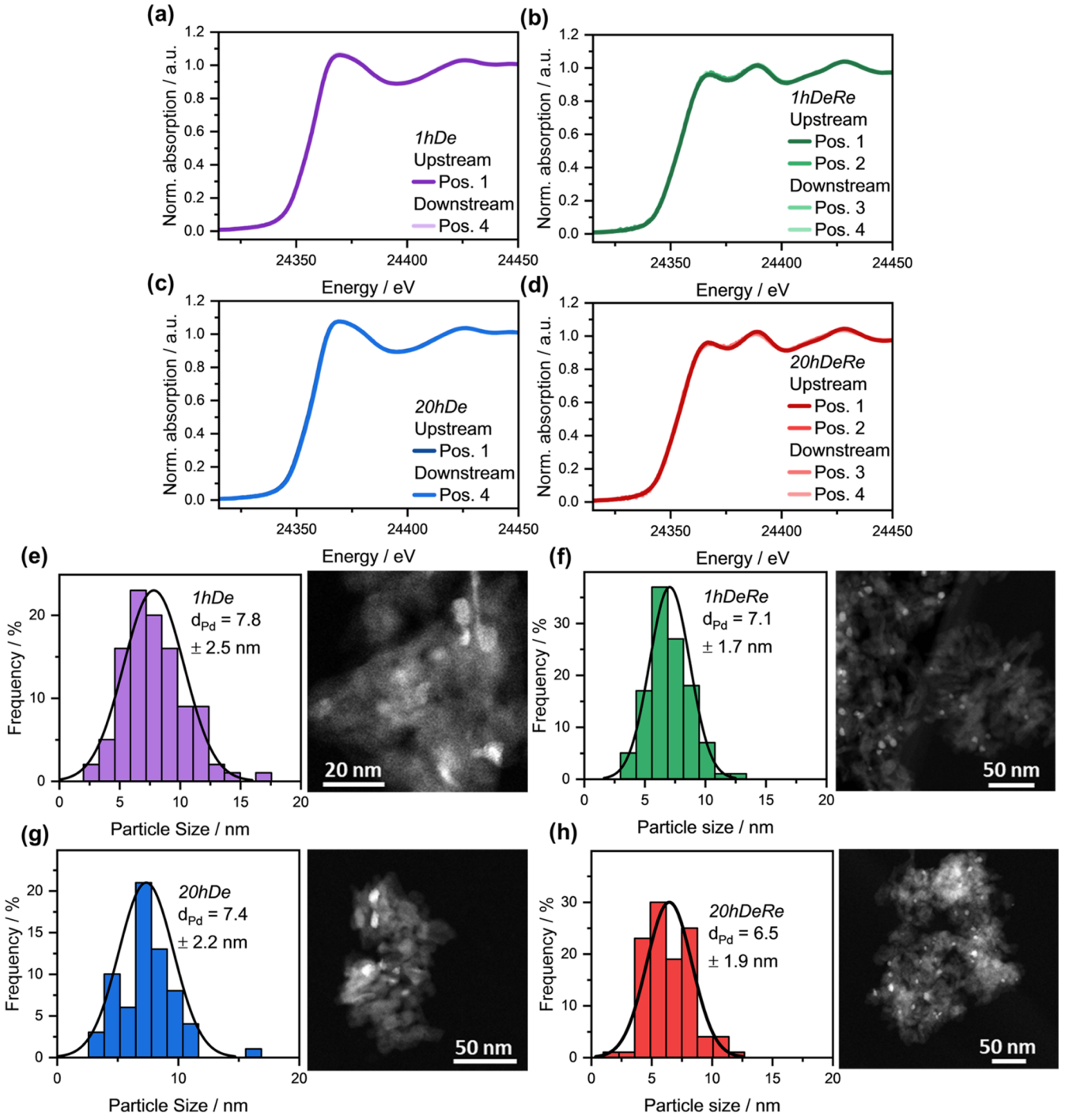

Figure 7. XANES analysis of deactivated and regenerated samples (a) *1hDe*, (b) *1hDeRe*, (c) *20hDe*, and (d) *20hDeRe* at the corresponding positions shown in Figure 6. (e–h) Particle size distributions and the corresponding HR-TEM images of the differently treated catalysts: (e) *1hDe*, (f) *1hDeRe*, (g) *20hDe*, and (h) *20hDeRe*. HR-TEM images of *0hDe* are provided in the Supporting Information (Figure S10).

spatial distribution of each component, allowing for the precise identification of the structural characteristics unique to each layer. However, the resolution obtained is not sufficient to directly visualize the presence and location of sulfur by thresholding and image segmentation. This would probably require resolution below 10 nm, which is not feasible on extended samples with current hard X-ray microscopy methods.[56,57] Nevertheless, holotomography has the advantage of providing a quantitative map of the local electron density (N_e) distribution, recovered from the phase shift values obtained in the reconstructed tomograms.[58] This property was exploited here to evaluate sulfur formation in terms of the variation in N_e within the sample. Typical cross sections of each sample based on grayscale N_e values are shown in Figure S15. The steps applied to convert the phase shift values to electron density are discussed in Section 6.2 of the Supporting Information.

Figure 8a shows the global N_e distribution within the whole sample of fresh Pd/Al_2O_3 (*F_in*). A peak around the lowest values was assigned to air in the macropores, while a second

https://doi.org/10.1021/acscatal.5c02678
ACS Catal. 2025, 15, 13470−13485

Table 3. Results of LCA for Regenerated Samples at the Pd KEge for *1hDeRe* and *20hDeRe* Located Up- and Downstream of the Catalyst[a]

	fraction of PdS/%	fraction of Pd/-	fraction of PdO/-
1hDeRe inlet, Pos. 1	20 ± 1.6	65 ± 2.2	15 ± 0.9
1hDeRe inlet, Pos. 2	24 ± 3.5	58 ± 4.2	16 ± 2.1
1hDeRe outlet, Pos. 3	24 ± 3.6	58 ± 4.3	18 ± 2.1
1hDeRe outlet, Pos. 4	21 ± 1.6	65 ± 2.2	14 ± 0.9
20hDeRe inlet, Pos. 1	27 ± 2.3	63 ± 2.9	10 ± 1.4
20hDeRe inlet, Pos. 2	36 ± 3.3	57 ± 4.0	7.0 ± 1.9
20hDeRe outlet, Pos. 3	34 ± 3.1	56 ± 3.8	10 ± 1.8
20hDeRe outlet, Pos. 4	39 ± 1.8	55 ± 2.5	6.0 ± 1.1

[a](Details of the LCA are given in the Supporting Information).

peak corresponds to the active material, *i.e.*, washcoat, and the third peak at higher N_e values to the cordierite support material.

Chemical speciation within structured catalysts is challenging if based purely on phase contrast imaging without the combination of additional contrast modes. This is because multiple chemical species with varying densities can form simultaneously in structured catalysts due to poisoning, leading to a highly heterogeneous distribution of chemical species.[59] At the same time, N_e changes may not necessarily originate only from sulfur stored in the washcoat but also from alternative factors such as changes in crystal structure or significant changes in pore size distribution, which have to be excluded. Since the conditions during the deactivation step were milder than during calcination/degreening, we can assume that changes in N_e observed are most likely a result of sulfur poisoning.[60,61] Despite these complexities, the data do allow for clear identification of the heterogeneous nature of the poisoning effects occurring within the monolithic structures, revealing spatial variation and structural differences across the sample.

For comparison purposes, the data sets should be normalized with respect to a single reference component. Although air is typically used as the reference, however, because the measurements were performed with local tomography, the limited presence of air prevented reliable normalization necessary to compare the absolute values of N_e of the washcoat. To mitigate this issue, further analysis was performed using not the absolute but the relative values of N_e following offsetting with respect to air. To do so, we considered the difference in N_e between the cordierite and washcoat maxima (α) as shown in Figure 8b, rather than comparing the absolute N_e of the washcoat itself. Any change in the chemical nature of the washcoat, which at the same time does not strongly affect the cordierite, in this case sulfur poisoning, will also reflect in the difference between the washcoat and cordierite maxima. This average difference ($\bar{\alpha}$) across each tomogram is provided in the Supporting Information for reference (Table S4). To utilize the spatial resolution of the tomographic data and examine the local variations within the sample, the analysis was performed on a slice-by-slice basis. Note that α for each slice number corresponds to the difference in the average of the N_e values for washcoat and cordierite voxels.

Since cordierite is assumed to remain unaffected by sulfur poisoning owing to its selection as the support, the increasing trend in the value of α in Figure 9 as *20hDe* < *1hDe* < *0hDe* signifies that there is an observable shift in the N_e value for the washcoat toward higher values (therefore decrease in α) as the time on stream for deactivation increases. This is particularly notable for the outlet position in Figure 9b compared to the inlet in Figure 9a. The trend aligns with the XRF data in Figure 5, which shows higher sulfur accumulation along the axial channel length in *20hDe* compared to *1hDe*. Moreover, the standard deviation of the peak difference values, shown in Table S5, is small compared to the magnitude of the observed shifts across all data sets. This nominal variation validates the statistical significance of the trend and the reliability of the observed shifts in N_e. Hence, it can be concluded that the changes in N_e for the washcoat are consistent and predominantly influenced by the time of exposure to sulfur poisoning, as also found by the XRF investigations in Figure 5.

Apart from axial variations, the radial behavior in the reactor, *i.e.*, along the thickness of the washcoat, is important. For the complex washcoated structure, different regions may be exposed to varying reaction conditions, depending on inlet or outlet position, heat and mass transport properties, and diffusion lengths, within localized regions of the washcoat. This further adds to the potential nonuniformity of the system. To analyze the local variations as a function of depth within the washcoat due to differences in material composition and localized reaction conditions, we focused on several regions of interest (ROIs). Such a comparison of the ROIs in the catalyst layer (Figure 10a) from the exterior to interior within the

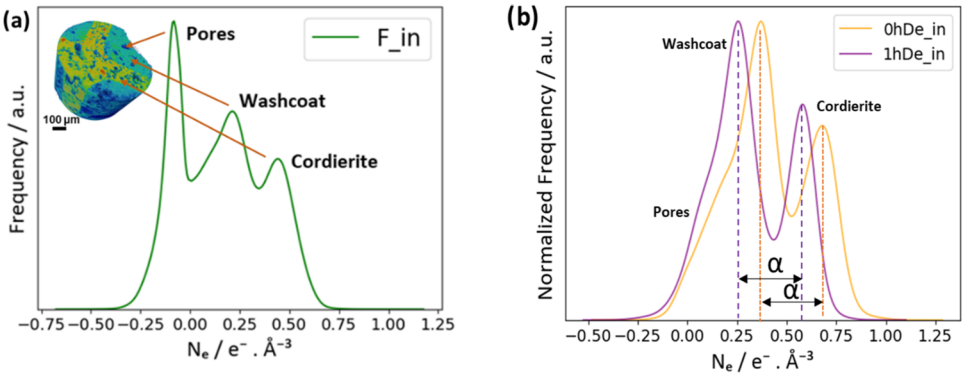

Figure 8. (a) Pictogram and histogram showing global N_e distribution of *F_in* sample, with 3 distinct features attributed to pores, washcoat material, and cordierite support. The increasing N_e values imply increasing bulk and/or volumetric density of cordierite with respect to the washcoat. (b) Global N_e distribution in *0hDe_in* and *1hDe_in* depicting the difference in N_e between the cordierite and washcoat maxima (α).

https://doi.org/10.1021/acscatal.5c02678
ACS Catal. 2025, 15, 13470−13485

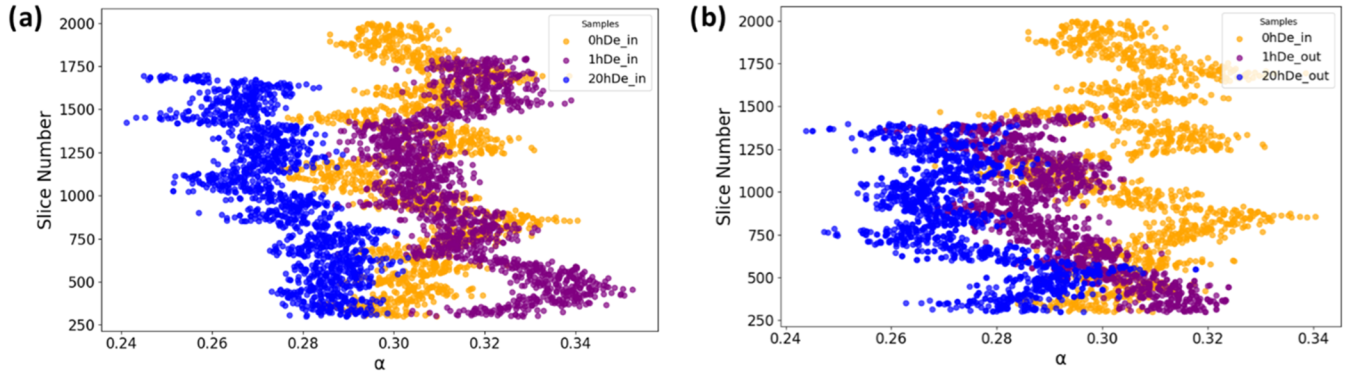

Figure 9. Plots of α *vs* slice number in the tomograms for samples *0hDe, 1hDe,* and *20hDe* inlets (a) and outlets (b).

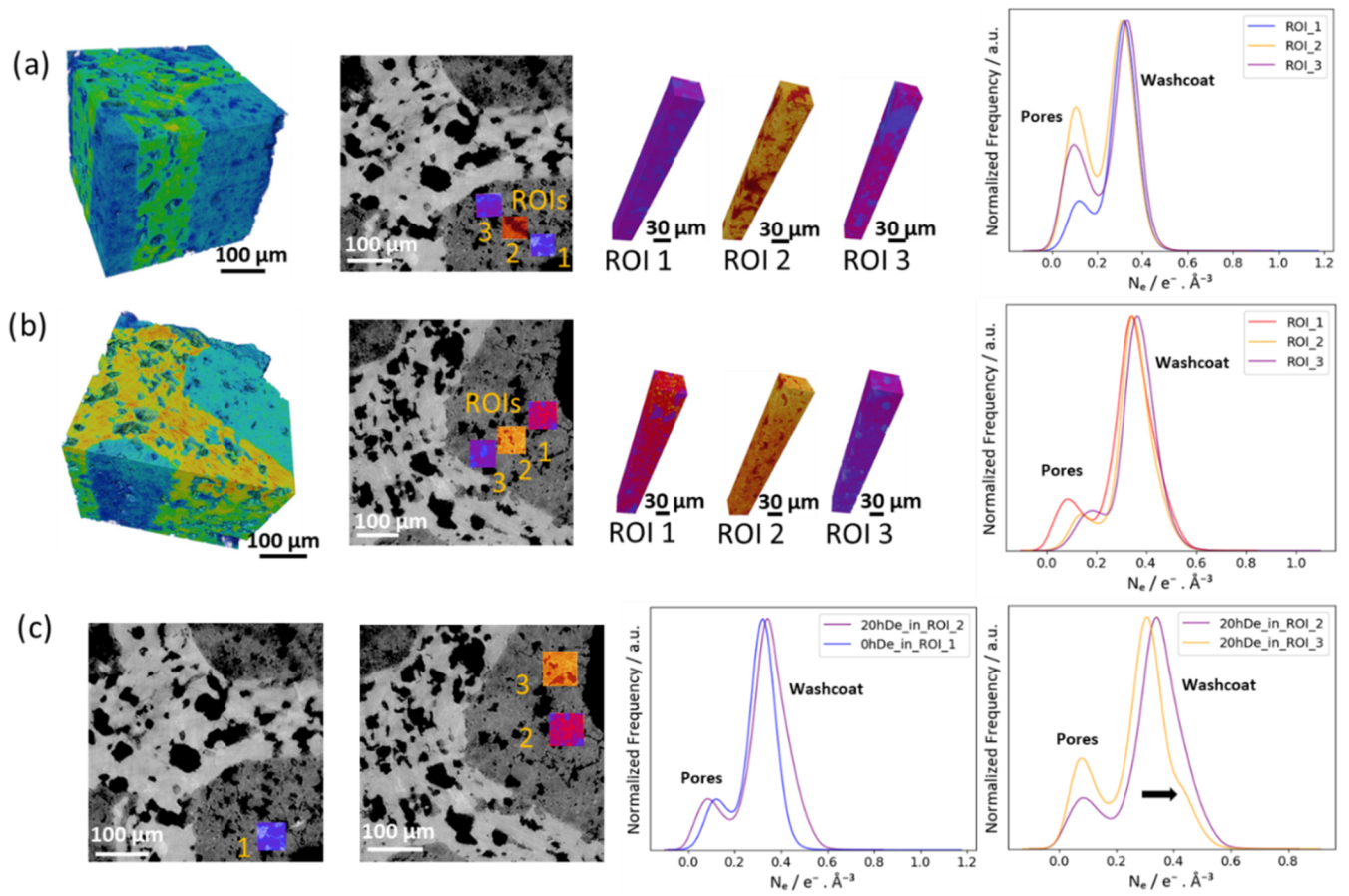

Figure 10. 3D volume, a 2D slice, 3D washcoat ROIs, N_e within ROIs for (a) *0hDe_in* and (b) *20hDe_in*. (c) Comparison between the N_e of ROIs from *0hDe_in* and *20hDe_in*.

washcoat of *0hDe_in* yields Gaussian peaks across all three positions, regardless of their specific location within the structure. The Gaussian fitting curves for these ROIs are provided in Figure S16. This suggests a certain degree of homogeneity in the electron density distribution throughout the sample, which is maintained despite exposure to the reaction conditions. Hence, during the degreening process at 550 °C, the system achieved a relatively uniform state.

In contrast, for *20hDe_in*, a comparison across three different positions in the catalyst layer reveals a non-Gaussian distribution in the corresponding histograms, as depicted in Figures 10b and S16. This deviation from the Gaussian shape highlights clear variations in electron density across these regions. The non-Gaussian profiles in each ROI reflect localized differences in material composition and structural changes within the washcoat, likely due to uneven exposure to reaction conditions and prolonged poisoning effects. This originates from the heterogeneous nature of the washcoat, mass transport limitations, and variations in reactant concentration within the porous structure. This variation in electron density across ROIs underscores the heterogeneous nature of the poisoning process at the inlet, suggesting the formation of high-density phases and chemical species unique to this section of the monolithic structure.

To further confirm the effects of the SO_2-poisoning in the outermost catalyst layer of the washcoat, we selected two

https://doi.org/10.1021/acscatal.5c02678
ACS Catal. 2025, 15, 13470−13485

positions from both *0hDe_in* (ROI 1 in Figure 10c) and *20hDe_in* (ROI 2 in Figure 10c). In this approach, it was ensured that each ROI was positioned equivalently within the monolithic structure, leading to equal exposure to reaction conditions. A marked contrast in the electron density distributions is observed: ROI 1 from *0hDe_in* displays a Gaussian distribution of the peaks corresponding to the pores and washcoat contributions, consistent with the homogeneous state of this sample. In contrast, ROI 2 from *20hDe_in* exhibits a distinctly non-Gaussian distribution with a broader peak with an extra shoulder toward higher values as indicated by the arrow for the catalyst washcoat, reflecting significant heterogeneity likely due to localized chemical or structural changes, probably connected to the presence of sulfur in the washcoat. This highlights the relative uniformity within *0hDe_in* compared to the more heterogeneous nature of *20hDe*.

To explore the variations within the outermost layer of the catalyst washcoat in *20hDe_in* itself, we selected two equally exposed ROIs (ROI 2 and 3 in Figure 10c) from similar regions and compared their electron density distributions. Despite being subjected to comparable reaction conditions, the two ROIs exhibit apparently different N_e profiles, as also depicted from the Gaussian fitting curve in Figure S16. Interestingly, the ROI with higher porosity also shows greater N_e variation, suggesting that the increased porosity may contribute to a more heterogeneous structural response to poisoning. The more porous region likely experiences greater exposure to the gas feed, and therefore more localized chemical reactions or species formation, further enhancing the variation in electron density. This comparison highlights how structural characteristics, such as porosity, can influence the degree of heterogeneity in electron density, emphasizing the complexity of the poisoning process within *20hDe*.

It can be concluded that the radial effects of sulfur poisoning depend on the physical structure of the washcoat at the specific location in both the axial and radial directions. On the one hand, this may reflect structural heterogeneity derived from sample preparation or the nature of the composite catalyst material. Additionally, this can be attributed to the presence of mesopores and smaller macropores within the sample that cannot be resolved through holotomography. On the other hand, the axial effects follow the trend of greater deviation from the fresh sample structure with increased deactivation time. Overall, although holotomography does not provide precise chemical contrast, it offers unique insights into the radial and axial trends related to the bulk and local structure, *i.e.*, both physical and chemical structures of the washcoat, which are not detectable through spatially resolved XANES or XRF. The observed trends with respect to deactivation time align well with other techniques, demonstrating the value of X-ray tomography in capturing structural variations within complex composite samples as a complementary analysis method.

3.5. Spatially Resolved CH_4 Conversion. Considering the sulfur gradients revealed by the XRF, the HT and XAS integral catalytic activity results cannot sufficiently represent the catalyst deactivation during operation. Hence, spatially resolved concentration profiles were determined for the different gas components during CH_4 oxidation. Figure 11 shows the CH_4 conversion as a function of the sampling position within the monolithic reactor for *0hDe*. The profile was recorded at a temperature leading to a CH_4 conversion of

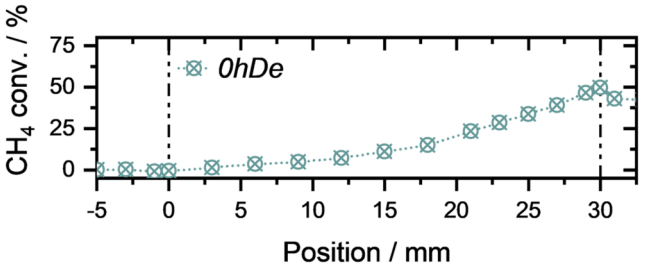

Figure 11. Spatially resolved activity profiles for methane oxidation at 50% CH_4 conversion in 3200 ppm of CH_4 and 10 vol % in N_2. The sample was degreened and tested for two light-offs with the addition of water in the gas feed.

ca. 50% under dry conditions (330 °C for *0hDe*), which shows an increase of methane consumption in axial direction with a higher activity downstream of the catalyst. For the sake of better comparison, the spatially resolved reaction rate in terms of turnover frequencies (TOFs) for the differently treated samples was calculated (a more detailed calculation is given in the Supporting Information). All profiles shown were recorded at 50% CH_4 conversion. Using the Arrhenius approach, the spatially resolved TOFs for the degreened sample (*0hDe*) were extrapolated to the temperatures at which the deactivated and regenerated samples were measured to also compare the increase in TOF.[62] The activation energy was derived from the initial light-off measurement under dry reaction conditions for the degreed and tested sample (*0hDe)*, prior to the spatially resolved measurements. The obtained value of 157 kJ mol^{-1} is well in line with literature data.[46] For the calculation of the TOF, the catalyst bed was divided into several sections, *e.g.*, from 0 to 2 mm. The TOFs have then been calculated based on the difference in conversion between each section and was normalized to the amount of Pd present in each section.

The spatially resolved TOFs for the differently treated catalysts, as well as the extrapolated TOFs for different temperatures, are depicted in Figure 12. Similar to the CH_4 conversion profile in Figure 11, the obtained TOF profiles for *0hDe* (Figure 12a–c, right) extrapolated to the temperatures 380, 430, and 360 °C show a stronger increase of the catalytic activity downstream of the monolith. While the shape of the TOF profile as a function of the axial position remains independent of the temperature, the order of magnitude increases with increasing temperature. For the last section of the catalyst bed, the TOF increases from 0.8 s^{-1} for 360 °C to 2.1 s^{-1} for 380 °C and to 16.4 s^{-1} for 430 °C. Figure 12a shows the axial TOF profile of *1hDe* obtained at 380 °C. The results exhibit a similar TOF profile compared to *0hDe* (Figure 12a, right). However, the TOF of *1hDe* is significantly smaller compared to *0hDe*: *e.g.*, for the last section, 0.2 s^{-1} for *1hDe* and 0.8 s^{-1} for *0hDe* (extrapolated to 380 °C). For *20hDeSpaci*, the axial TOF profile (Figure 12b, left) becomes almost constant along the catalyst bed with a slight increase toward the outlet. Compared to the *0hDe* counterpart shown in Figure 12b (right), the TOFs are smaller by over an order of magnitude. Lastly, the axial profile changes again after the regeneration step is applied (Figure 12c, left): The axial profile becomes a mixture of the *0hDe* and *20hDeSpaci*, as the TOF profile is almost linear until the middle of the catalyst bed but does increase more downstream.

The minor changes in the axial TOF profile of *1hDe* (Figure 12a) are likely due to the onset of SO_2-poisoning upstream of

https://doi.org/10.1021/acscatal.5c02678
ACS Catal. 2025, 15, 13470−13485

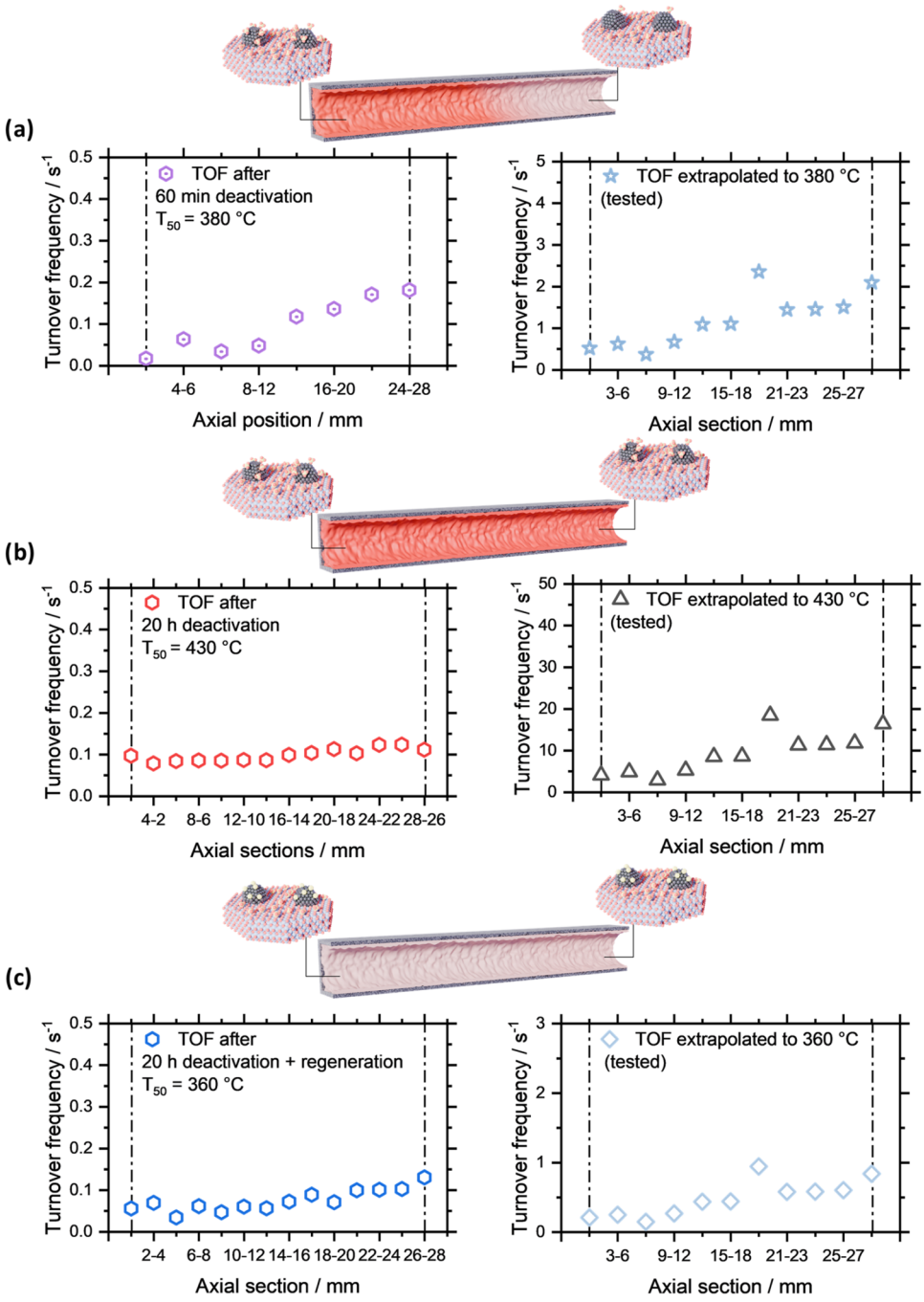

Figure 12. Spatially resolved TOF for each axial section normalized to the Pd surface for CH_4 oxidation at 50% conversion in a gas atmosphere containing 3200 ppm of CH_4 and 10 vol % in N_2. (a) Spatially resolved TOF after 1 h deactivation (left, T_{50} = 380 °C), the TOF of the tested sample (right, extrapolated to 380 °C), and schematic of S distribution along the monolith channel. (b) Spatially resolved TOF after 20 h deactivation (left, T_{50} = 430 °C), the TOF of the tested sample (right, extrapolated to 430 °C), and schematic of S distribution along the monolith channel. (c) Spatially resolved TOF after 60 h deactivation +5 min regeneration at 450 °C in 2 vol % H_2 (left, T_{50} = 360 °C), the TOF of the tested sample (right, extrapolated to 360 °C), and schematic of S distribution along the monolith channel.

the honeycomb, which is underlined by the smaller slope compared to *0hDe*. This observation is also in line with the observed XRF S profiles, S K-edge spectra, and the integral reaction rate (Figures 3, 5, and 6). With the advancing S poisoning throughout the monolithic honeycomb, the TOF profile starts to flatten, resulting in a more linear slope (*20hDeSpaci*). Simultaneously, the reaction rate approaches a minimum (Figure 5), indicating a low overall catalytic activity throughout the honeycomb. The linear TOF profile can be partially reversed by H_2 regeneration, resulting in the TOF profile becoming more similar to *0hDe*, accompanied by an increase in catalytic activity.

4. CONCLUSIONS

By systematically changing the exposure time of washcoated Pd/Al_2O_3 catalysts to sulfur species in terms of SO_2 during methane oxidation, we were able to capture the strong deactivation effect of sulfur on the catalytic activity, especially

https://doi.org/10.1021/acscatal.5c02678
ACS Catal. 2025, 15, 13470−13485

compared to H_2O deactivation. Complementary spectroscopic, microscopic, and catalytic studies depict a situation in which poisoning starts at the inlet of the catalyst bed or monolith channel and progresses toward the end. The catalytic activity could be mostly or partially recovered with a regenerative treatment in a reducing atmosphere. However, this effect diminished with a longer exposure to sulfur. The effect of sulfur poisoning was also reflected by spatially resolved kinetic measurements of predeactivated samples with different slopes of their turnover frequency as a function of deactivation time. These local catalytic measurements can, therefore, give indirect information on the degree of poisoning in the catalyst bed or monolithic channel. The effect of sulfur needed analysis on different length scales. On the meso scale, XRF analysis revealed spatially resolved sulfur gradients along the technical catalysts as a function of deactivation time and subsequent regeneration treatment, which were further quantified and confirmed by elemental analysis. The analysis together with holotomography showed higher amounts of S stored upstream of the catalyst bed, which also persisted after the regeneration treatment. On the meso scale, holotomography revealed local variations of sulfur on the washcoated Pd/Al_2O_3 catalyst due to its inherent heterogeneity but not specifically in the radial direction. A more systematic application of holotomography with defined regions of the samples and possibly higher resolution will further allow us to resolve trends in the heterogeneous chemical composition observed. On the atomic scale, XAS at the S K-edge showed that S^{6+} was the predominant oxidation state of sulfur even after regeneration. Complementary XAS at the Pd K-edge revealed no significant gradients in the oxidation state following the regeneration. However, XAS analysis at the Pd L_3-edge following the deactivation treatment suggested pronounced gradients of Pd−S species along the coated catalyst. The observed gradient was further proven by the differential catalytic activity measurements, which showed a change in slope for the CH_4 activity profile together with a significant decrease in catalytic activity and may therefore serve as a tool in technical applications.

■ ASSOCIATED CONTENT

Data Availability Statement

X-ray absorption spectroscopy at the Pd and S K-edge, X-ray fluorescence analysis and catalytic activity for this paper are available on KITOpen at: 10.35097/ftrca4n1zbfbmjvy. The raw data of the X-ray holotomography is available under: https://doi.esrf.fr/10.15151/ESRF-DC-2199982139.

Supporting Information

The Supporting Information is available free of charge at https://pubs.acs.org/doi/10.1021/acscatal.5c02678.

Detailed information on supplementary characterization data, holotomography, TOF calculations, and X-ray absorption spectroscopy (PDF)

■ AUTHOR INFORMATION

Corresponding Authors

Thomas L. Sheppard − *Institute for Chemical Technology and Polymer Chemistry (ITCP), Karlsruhe Institute of Technology (KIT), Karlsruhe 76131, Germany;* Present Address: Institute of Chemical Technologies and Analytics (CTA), TU Wien, Vienna 1060, Austria; orcid.org/0000-0002-8891-985X; Email: thomas.sheppard@tuwien.ac.at

Jan-Dierk Grunwaldt − *Institute for Chemical Technology and Polymer Chemistry (ITCP), Karlsruhe Institute of Technology (KIT), Karlsruhe 76131, Germany; Institute of Catalysis Research and Technology (IKFT), Karlsruhe Institute of Technology (KIT), Karlsruhe 76344, Germany;* orcid.org/0000-0003-3606-0956; Email: grunwaldt@kit.edu

Authors

Tim Delrieux − *Institute for Chemical Technology and Polymer Chemistry (ITCP), Karlsruhe Institute of Technology (KIT), Karlsruhe 76131, Germany;* orcid.org/0009-0006-1923-495X

Shweta Sharma − *Institute for Chemical Technology and Polymer Chemistry (ITCP), Karlsruhe Institute of Technology (KIT), Karlsruhe 76131, Germany;* orcid.org/0000-0002-0355-176X

Florian Maurer − *Institute for Chemical Technology and Polymer Chemistry (ITCP), Karlsruhe Institute of Technology (KIT), Karlsruhe 76131, Germany;* orcid.org/0000-0002-3307-4132

Joachim Czechowsky − *Institute for Chemical Technology and Polymer Chemistry (ITCP), Karlsruhe Institute of Technology (KIT), Karlsruhe 76131, Germany;* orcid.org/0009-0000-3741-2410

Camelia Nicoleta Borca − *Paul Scherrer Institute (PSI), Villigen 5232, Switzerland*

Dmitry Karpov − *European Synchrotron Radiation Facility (ESRF), Grenoble 38000, France*

Camilo Cárdenas − *Institute for Chemical Technology and Polymer Chemistry (ITCP), Karlsruhe Institute of Technology (KIT), Karlsruhe 76131, Germany;* orcid.org/0009-0008-3261-9947

Patrick Lott − *Institute for Chemical Technology and Polymer Chemistry (ITCP), Karlsruhe Institute of Technology (KIT), Karlsruhe 76131, Germany;* orcid.org/0000-0001-8683-2155

Maria Casapu − *Institute for Chemical Technology and Polymer Chemistry (ITCP), Karlsruhe Institute of Technology (KIT), Karlsruhe 76131, Germany;* orcid.org/0000-0002-8755-9856

Complete contact information is available at: https://pubs.acs.org/10.1021/acscatal.5c02678

Author Contributions

[⊥]T.D. and S.S. contributed equally to this work.

Notes

The authors declare no competing financial interest.

■ ACKNOWLEDGMENTS

This study was funded by the Deutsche Forschungsgemeinschaft (DFG, German Research Foundation)−SFB 1441−Project-ID 426888090 (projects C02 and C03). The authors would like to thank A. Zimina (IKFT, KIT) for their assistance during and providing beamtime at the CatAct beamline (KIT Light Source), ESRF for beamtime at ID16A to carry out tomography measurements (proposal ID: CH-6482), Dr. Mikhail Lyubomirskiy (DESY), Dr. Tang Li (DESY), Leonardo de Campos (ITCP, KIT) for assistance during the beamtime, L. Braun (ITCP, KIT) for the XRD analysis, T. Eldrige (IKFT, KIT) for the BET analysis, and C. Maliakkal (INT, KIT) for the TEM measurements. We acknowledge the

Paul Scherrer Institut, Villigen, Switzerland, for the provision of synchrotron radiation beamtime at the PHOENIX beamline for the XRF spectra and part of the XAS measurements. This work was partly carried out with the support of the Karlsruhe Nano Micro Facility (KNMFi, www.knmf.kit.edu), a Helmholtz Research Infrastructure at Karlsruhe Institute of Technology (KIT, www.kit.edu). The authors thank DAPHNE4NFDI (DFG project under project number 460248799) as well as further NFDI-consortia (NFDI4Cat, FAIRMAT and NFDI4Chem) for fruitful discussion and valuable input for implementing FAIR data principles in this work. The authors also thank O. Deutschmann (ITCP, KIT) for the provision of infrastructure and equipment and fruitful discussion.

REFERENCES

(1) Cho, H. M.; He, B. Q. Spark ignition natural gas engines—A review. *Energy Convers. Manage.* **2007**, *48*, 608−618.
(2) Wahbi, A.; Tsolakis, A.; Herreros, J.*Emissions Control Technologies for Natural Gas Engines*, Energy, Environment, and Sustainability; Springer, 2019; Vol. *359*, p 379.
(3) Hesterberg, T. W.; Lapin, C. A.; Bunn, W. B. A comparison of emissions from vehicles fueled with diesel or compressed natural gas. *Environ. Sci. Technol.* **2008**, *42*, 6437−6445.
(4) Lott, P.; Deutschmann, O. Lean-Burn Natural Gas Engines: Challenges and Concepts for an Efficient Exhaust Gas Aftertreatment System. *Emiss. Control Sci. Technol.* **2021**, *7*, 1−6.
(5) Yu, Z.; Schanbacher, F. L. Production of Methane Biogas as Fuel Through Anaerobic Digestion. *Sustainable Biotechnol.* **2010**, 105−127.
(6) Ghaib, K.; Ben-Fares, F. Z. Power-to-Methane: A state-of-the-art review. *Renewable Sustainable Energy Rev.* **2018**, *81*, 433−446.
(7) Boucher, O.; Friedlingstein, P.; Collins, B.; Shine, K. P. The indirect global warming potential and global temperature change potential due to methane oxidation. *Environ. Res. Lett.* **2009**, *4*, No. 044007.
(8) Burch, R.; Urbano, F. J. Investigation of the Active State of Supported Palladium Catalysts in the Combustion of Methane. *Appl. Catal. A* **1995**, *124*, 121−138.
(9) Burch, R.; Urbano, F. J. Investigation of the active state of supported palladium catalysts in the combustion of methane. *Appl. Catal. A* **1995**, *124*, 121−138.
(10) Deutschmann, O.; Grunwaldt, J.-D. Exhaust gas aftertreatment in mobile systems: status, challenges, and perspectives. *Chem. Ing. Tech.* **2013**, *85*, 595−617.
(11) Ciuparu, D.; Lyubovsky, M. R.; Altman, E.; Pfefferle, L. D.; Datye, A. Catalytic combustion of methane over palladium-based catalysts. *Catal. Rev.* **2002**, *44*, 593−649.
(12) Lott, P.; Casapu, M.; Grunwaldt, J.-D.; Deutschmann, O. A review on exhaust gas after-treatment of lean-burn natural gas engines—From fundamentals to application. *Appl. Catal. B* **2024**, *340*, No. 123241.
(13) Argyle, M. D.; Bartholomew, C. H. Heterogeneous catalyst deactivation and regeneration: a review. *Catalysts* **2015**, *5*, 145−269.
(14) Lott, P.; Eck, M.; Doronkin, D. E.; Zimina, A.; Tischer, S.; Popescu, R.; Belin, S.; Briois, V.; Casapu, M.; Grunwaldt, J.-D.; Deutschmann, O. Understanding sulfur poisoning of bimetallic Pd-Pt methane oxidation catalysts and their regeneration. *Appl. Catal. B* **2020**, *278*, No. 119244.
(15) Keller, K.; Lott, P.; Stotz, H.; Maier, L.; Deutschmann, O. Microkinetic Modeling of the Oxidation of Methane Over PdO Catalysts—Towards a Better Understanding of the Water Inhibition Effect. *Catalysts* **2020**, *10*, No. 922.
(16) Coney, C.; Stere, C.; Millington, P.; Raj, A.; Wilkinson, S.; Caracotsios, M.; McCullough, G.; Hardacre, C.; Morgan, K.; Thompsett, D.; Goguet, A. Spatially-resolved investigation of the water inhibition of methane oxidation over palladium. *Catal. Sci. Technol.* **2020**, *10*, 1858−1874.
(17) Kikuchi, R.; Maeda, S.; Sasaki, K.; Wennerström, S.; Eguchi, K. Low-temperature methane oxidation over oxide-supported Pd catalysts: inhibitory effect of water vapor. *Appl. Catal. A* **2002**, *232*, 23−28.
(18) Monai, M.; Montini, T.; Melchionna, M.; Duchoň, T.; Kúš, P.; Chen, C.; Tsud, N.; Nasi, L.; Prince, K. C.; Veltruská, K.; Matolín, V.; Khader, M. M.; Gorte, R. J.; Fornasiero, P. The effect of sulfur dioxide on the activity of hierarchical Pd-based catalysts in methane combustion. *Appl. Catal. B* **2017**, *202*, 72−83.
(19) Hamzehlouyan, T.; Sampara, C.; Li, J.; Kumar, A.; Epling, W. Sulfur Poisoning of a Pt/Al_2O_3 Oxidation Catalyst: Understanding of SO_2, SO_3 and H_2SO_4 Impacts. *Top. Catal.* **2016**, *59*, 1028−1032.
(20) Sadokhina, N.; Smedler, G.; Nylén, U.; Olofsson, M.; Olsson, L. Deceleration of SO_2 poisoning on $PtPd/Al_2O_3$ catalyst during complete methane oxidation. *Appl. Catal. B* **2018**, *236*, 384−395.
(21) Hu, L. R.; Williams, S. Sulfur poisoning and regeneration of Pd catalyst under simulated emission conditions of natural gas engine. *SAE Trans.* **2007**, 909−917.
(22) Summers, J. C. Reaction of Sulfur Oxides with Alumina and Platinum/Alumina. *Environ. Sci. Technol.* **1979**, *13*, 321−325.
(23) Gremminger, A.; Lott, P.; Merts, M.; Casapu, M.; Grunwaldt, J.-D.; Deutschmann, O. Sulfur poisoning and regeneration of bimetallic Pd-Pt methane oxidation catalysts. *Appl. Catal. B* **2017**, *218*, 833−843.
(24) Lott, P.; Eck, M.; Doronkin, D. E.; Popescu, R.; Casapu, M.; Grunwaldt, J.-D.; Deutschmann, O. Regeneration of Sulfur Poisoned $Pd-Pt/CeO_2 - ZrO_2 - Y_2O_3 - La_2O_3$ and $Pd-Pt/Al_2O_3$ Methane Oxidation Catalysts. *Top. Catal.* **2019**, *62*, 164−171.
(25) Lott, P.; Casapu, M.; Grunwaldt, J.-D.; Deutschmann, O. A review on exhaust gas after-treatment of lean-burn natural gas engines—From fundamentals to application. *Appl. Catal. B* **2024**, *340*, No. 123241.
(26) Nissinen, V. H.; Kinnunen, N. M.; Suvanto, M. Regeneration of a sulfur-poisoned methane combustion catalyst: Structural evidence of Pd_4S formation. *Appl. Catal. B* **2018**, *237*, 110−115.
(27) Hamzehlouyan, T.; Sampara, C. S.; Li, J.; Kumar, A.; Epling, W. S. Kinetic study of adsorption and desorption of SO_2 over γ-Al_2O_3 and Pt/γ-Al_2O_3. *Appl. Catal. B* **2016**, *181*, 587−598.
(28) Delrieux, T.; Sharma, S.; Maurer, F.; Dolcet, P.; Lausch, M.; Zimina, A.; Cárdenas, C.; Lott, P.; Casapu, M.; Sheppard, T. L.; Grunwaldt, J.-D. A laboratory scale fast feedback characterization loop for optimizing coated catalysts for emission control. *React. Chem. Eng.* **2024**, *9*, 2868−2881.
(29) Livio, D.; Diehm, C.; Donazzi, A.; Beretta, A.; Deutschmann, O. Catalytic partial oxidation of ethanol over Rh/Al_2O_3: Spatially resolved temperature and concentration profiles. *Appl. Catal. A* **2013**, *467*, 530−541.
(30) Hlavatý, T.; Kočí, P.; Isoz, M.; Deka, D.; Partridge, W. Balanced Fast-SpaciMS capillary configurations provide practically noninvasive channel-average measurements in catalytic monoliths. *Chem. Eng. Sci.* **2023**, *282*, No. 119272.
(31) Brunauer, S.; Emmett, P. H.; Teller, E. Adsorption of Gases in Multimolecular Layers. *J. Am. Chem. Soc.* **1938**, *60*, 309−319.
(32) Barrett, E. P.; Joyner, L. G.; Halenda, P. P. The Determination of Pore Volume and Area Distributions in Porous Substances. I. Computations from Nitrogen Isotherms. *J. Am. Chem. Soc.* **1951**, *73*, 373−380.
(33) Schindelin, J.; Arganda-Carreras, I.; Frise, E.; Kaynig, V.; Longair, M.; Pietzsch, T.; Preibisch, S.; Rueden, C.; Saalfeld, S.; Schmid, B.; Tinevez, J. Y.; White, D. J.; Hartenstein, V.; Eliceiri, K.; Tomancak, P.; Cardona, A. Fiji: an open-source platform for biological-image analysis. *Nat. Methods* **2012**, *9*, 676−682.
(34) Kim, G.; Hugonnet, H.; Kim, K.; Lee, J. H.; Lee, S. S.; Ha, J.; Lee, C.; Park, H.; Yoon, K. J.; Shin, Y.; Csucs, G.; Hitchcock, I.; Mackinder, L.; Kim, J. H.; Hwang, T. H.; Lee, S.; O'Toole, P.; Koo, B. K.; Guck, J.; Park, Y. K. Holotomography. *Nat. Rev. Methods Primers* **2024**, *4*, No. 51.
(35) Paganin, D.; Mayo, S. C.; Gureyev, T. E.; Miller, P. R.; Wilkins, S. W. Simultaneous phase and amplitude extraction from a single

https://doi.org/10.1021/acscatal.5c02678
ACS Catal. 2025, 15, 13470−13485

defocused image of a homogeneous object. *J. Microsc.* **2002**, *206*, 33−40.
(36) Diaz, A.; Trtik, P.; Guizar-Sicairos, M.; Menzel, A.; Thibault, P.; Bunk, O. Quantitative x-ray phase nanotomography. *Phys. Rev. B* **2012**, *85*, No. 020104.
(37) Dierolf, M.; Menzel, A.; Thibault, P.; Schneider, P.; Kewish, C. M.; Wepf, R.; Bunk, O.; Pfeiffer, F. Ptychographic X-ray computed tomography at the nanoscale. *Nature* **2010**, *467*, 436−439.
(38) Zimina, A.; Dardenne, K.; Denecke, M. A.; Doronkin, D. E.; Huttel, E.; Lichtenberg, H.; Mangold, S.; Pruessmann, T.; Rothe, J.; Spangenberg, T.; Steininger, R.; Vitova, T.; Geckeis, H.; Grunwaldt, J.-D. CAT-ACT-A new highly versatile x-ray spectroscopy beamline for catalysis and radionuclide science at the KIT synchrotron light facility ANKA. *Rev. Sci. Instrum.* **2017**, *88*, No. 113113.
(39) Newville, M. IFEFFIT: interactive XAFS analysis and FEFF fitting. *Synchrotron Radiat.* **2001**, *8*, 322−324.
(40) Lott, P.; Dolcet, P.; Casapu, M.; Grunwaldt, J.-D.; Deutschmann, O. The effect of prereduction on the performance of Pd/Al_2O_3 and Pd/CeO_2 catalysts during methane oxidation. *Ind. Eng. Chem. Res.* **2019**, *58*, 12561−12570.
(41) Ciuparu, D.; Pfefferle, L. Support and water effects on palladium based methane combustion catalysts. *Appl. Catal. A* **2001**, *209*, 415−428.
(42) Van Giezen, J. C.; van den Berg, F. R.; Kleinen, J. L.; Van Dillen, A. J.; Geus, J. W. The effect of water on the activity of supported palladium catalysts in the catalytic combustion of methane. *Catal. Today* **1999**, *47*, 287−293.
(43) Boubnov, A.; Gremminger, A.; Casapu, M.; Deutschmann, O.; Grunwaldt, J.-D. Dynamics of the Reversible Inhibition during Methane Oxidation on Bimetallic Pd-Pt Catalysts Studied by Modulation-Excitation XAS and DRIFTS. *ChemCatChem* **2022**, *14*, No. e202200573.
(44) Liu, R. J.; Crozier, P. A.; Smith, C. M.; Hucul, D. A.; Blackson, J.; Salaita, G. Metal sintering mechanisms and regeneration of palladium/alumina hydrogenation catalysts. *Appl. Catal. A* **2005**, *282*, 111−121.
(45) Franken, T.; Roger, M.; Petrov, A. W.; Clark, A. H.; Agote-Arán, M.; Krumeich, F.; Kröcher, O.; Ferri, D. Effect of Short Reducing Pulses on the Dynamic Structure, Activity, and Stability of Pd/Al_2O_3 for Wet Lean Methane Oxidation. *ACS Catal.* **2021**, *11*, 4870−4879.
(46) Keller, K.; Hodonj, D.; Zeh, L.; Caulfield, L.; Sauter, E.; Wöll, C.; Deutschmann, O.; Lott, P. Spatiotemporal insights into forced dynamic reactor operation for fast light-off of Pd-based methane oxidation catalysts. *Catal. Sci. Technol.* **2024**, *14*, 4142−4153.
(47) Chenakin, S. P.; Melaet, G.; Szukiewicz, R.; Kruse, N. XPS study of the surface chemical state of a $Pd/(SiO_2 + TiO_2)$ catalyst after methane oxidation and SO2 treatment. *J. Catal.* **2014**, *312*, 1−11.
(48) Lampert, J. K.; Kazi, M. S.; Farrauto, R. J. Palladium catalyst performance for methane emissions abatement from lean burn natural gas vehicles. *Appl. Catal. B* **1997**, *14*, 211−223.
(49) Hamzehlouyan, T.; Sampara, C. S.; Li, J.; Kumar, A.; Epling, W. S. Kinetic study of adsorption and desorption of SO_2 over γ-Al_2O_3 and Pt/γ-Al_2O_3. *Appl. Catal. B* **2016**, *181*, 587−598.
(50) Venezia, A. M.; Murania, R.; Pantaleo, G.; Deganello, G. Pd and PdAu on mesoporous silica for methane oxidation: Effect of SO_2. *J. Catal.* **2007**, *251*, 94−102.
(51) Venezia, A. M.; Murania, R.; Pantaleo, G.; Deganello, G. Pd and PdAu on mesoporous silica for methane oxidation: Effect of SO_2. *J. Catal.* **2007**, *251*, 94−102.
(52) Kim, D. H.; Kwak, J. H.; Szanyi, J.; Cho, S. J.; Peden, C. H. F. Roles of Pt and BaO in the sulfation of $Pt/BaO/Al_2O_3$ lean NOx trap materials: Sulfur K-edge XANES and Pt LIII XAFS studies. *J. Phys. Chem. C* **2008**, *112*, 2981−2987.
(53) Kim, D. H.; Kwak, J. H.; Szanyi, J.; Cho, S. J.; Peden, C. H. F. Roles of Pt and BaO in the sulfation of $Pt/BaO/Al_2O_3$ lean NOx trap materials: Sulfur K-edge XANES and Pt LIII XAFS studies. *J. Phys. Chem. C* **2008**, *112*, 2981−2987.
(54) Orduz, H. A. S.; Bugarin, L.; Heck, S.-L.; Dolcet, P.; Casapu, M.; Grunwaldt, J.-D.; Glatzel, P. x-ray spectroscopy for functional materials L_3-edge X-ray spectroscopy of rhodium and palladium compounds. *J. Synchrotron Radiat.* **2024**, *31*, 733−740.
(55) Werny, M. J.; Valadian, R.; Lohse, L. M.; Robisch, A. L.; Zanoni, S.; Hendriksen, C.; Weckhuysen, B. M.; Meirer, F. X-ray nanotomography uncovers morphological heterogeneity in a polymerization catalyst at multiple reaction stages. *Chem. Catal.* **2021**, *1*, 1413−1426.
(56) Cloetens, P.; Ludwig, W.; Baruchel, J.; Van Dyck, D.; Van Landuyt, J.; Guigay, J. P.; Schlenker, M. Holotomography: Quantitative phase tomography with micrometer resolution using hard synchrotron radiation x rays. *Appl. Phys. Lett.* **1999**, *75*, 2912−2914.
(57) Diaz, A.; Trtik, P.; Guizar-Sicairos, M.; Menzel, A.; Thibault, P.; Bunk, O. Quantitative x-ray Phase Nanotomography. *Phys. Rev. B* **2012**, *85*, No. 020104(R).
(58) Diaz, A.; Trtik, P.; Guizar-Sicairos, M.; Menzel, A.; Thibault, P.; Bunk, O. Quantitative x-ray phase nanotomography. *Phys. Rev. B* **2012**, *85*, No. 020104(R).
(59) Veselý, M.; Valadian, R.; Lohse, L. M.; Toepperwien, M.; Spiers, K.; Garrevoet, J.; Vogt, E. T. C.; Salditt, T.; Weckhuysen, B. M.; Meirer, F. 3-D X-ray Nanotomography Reveals Different Carbon Deposition Mechanisms in a Single Catalyst Particle. *ChemCatChem* **2021**, *13*, 2494−2507.
(60) Weber, S.; Batey, D.; Cipiccia, S.; Stehle, M.; Abel, K. L.; Gläser, R.; Sheppard, T. L. Hard X-Ray Nanotomography for 3D Analysis of Coking in Nickel-Based Catalysts. *Angew. Chem., Int. Ed.* **2021**, *60*, 21772−21777.
(61) Weber, S.; Karpov, D.; Kahnt, M.; Diaz, A.; Romanenko, Y.; Kotrel, S.; Haas, A.; Hinrichsen, B.; Bottke, N.; Grunwaldt, J.-D.; Schunk, S.; Sheppard, T. L. Multimodal Hard X-Ray Nanotomography Probes Pore Accessibility of Technical Catalysts after Coking. *ChemCatChem* **2024**, *16*, No. e202301298.
(62) Chorkendorff, I.; Niemantsverdriet, J. W. *Concepts of Modern Catalysis and Kinetics*, 2nd ed.; Wiley, 2003.

https://doi.org/10.1021/acscatal.5c02678
ACS Catal. 2025, 15, 13470−13485